Journal of Coordination Chemistry

ISSN: 0095-8972 (Print) 1029-0389 (Online) Journal homepage: www.tandfonline.com/journals/gcoo20

The role of *N,N*-chelate ligand on the reactivity of (η^6-*p*-cymene)Ru(II) complexes: kinetics, DNA and protein interaction studies

Gershom Kyalo Mutua, Rajesh Bellam, Deogratius Jaganyi & Allen Mambanda

To cite this article: Gershom Kyalo Mutua, Rajesh Bellam, Deogratius Jaganyi & Allen Mambanda (2019) The role of *N,N*-chelate ligand on the reactivity of (η^6-*p*-cymene)Ru(II) complexes: kinetics, DNA and protein interaction studies, Journal of Coordination Chemistry, 72:17, 2931-2956, DOI: 10.1080/00958972.2019.1676893

To link to this article: https://doi.org/10.1080/00958972.2019.1676893

JOURNAL OF COORDINATION CHEMISTRY
2019, VOL. 72, NO. 17, 2931–2956
https://doi.org/10.1080/00958972.2019.1676893

Taylor & Francis
Taylor & Francis Group

The role of *N,N*-chelate ligand on the reactivity of (η^6-*p*-cymene)Ru(II) complexes: kinetics, DNA and protein interaction studies

Gershom Kyalo Mutua[a,b], Rajesh Bellam[a], Deogratius Jaganyi[c,d] and Allen Mambanda[a]

[a]School of Chemistry and Physics, University of KwaZulu-Natal, Scottsville, Pietermaritzburg, South Africa; [b]Department of Pure and Applied Chemistry, Masinde Muliro University of Science and Technology, Kakamega, Kenya; [c]School of Science, College of Science and Technology, University of Rwanda, Kigali, Rwanda; [d]Department of Chemistry, Faculty of Applied Sciences, Durban University of Technology, Durban, South Africa

ABSTRACT

This study reports the kinetic studies of aqua complexes (**Ru1–Ru6**) as well as the calf-thymus DNA (CT-DNA) and bovine serum albumin binding studies of their chloro derivatives (**Ru7–Ru11**). The rate of substitution of the aqua ligand(s) in **Ru1**–**Ru6** by thiourea nucleophiles (thiourea, *N,N*-dimethylthiourea and *N,N,N′,N′*-tetramethylthiourea) in 0.1 M $HClO_4/NaClO_4$ aqueous medium was investigated as a function of nucleophile concentration and temperature under *pseudo*-first order conditions. The reactivity of the binuclear and mononuclear complexes decreased in the order **Ru3** > **Ru4** > **Ru5** > **Ru6** and **Ru1** > **Ru2**, respectively. The trend in reactivity of the binuclear complexes showed a dependence on the electronic and static factors of the rigid N,N-chelate bridging ligand in the complexes. The reactivity trends are well supported by the DFT-calculated data. The activation parameters ($\Delta H^{\neq} > 0$, $\Delta S^{\neq} < 0$) for the substitution process in all complexes support an associative mechanism of activation. The complexes effectively bind to CT-DNA *via* intercalation and this was corroborated by the molecular docking results. Likewise, the complexes bind favorably with bovine serum albumin. The order of CT-DNA and bovine serum albumin interactions with these complexes are in line with the trends in aqua ligand substitution.

ARTICLE HISTORY
Received 8 June 2019
Accepted 20 September 2019

KEYWORDS
Ruthenium; kinetics; substitution; thiourea; nucleophile; binding; CT-DNA; bovine serum albumin

CONTACT Deogratius Jaganyi deojaganyi@gmail.com

Supplementary material for this article can be accessed here.

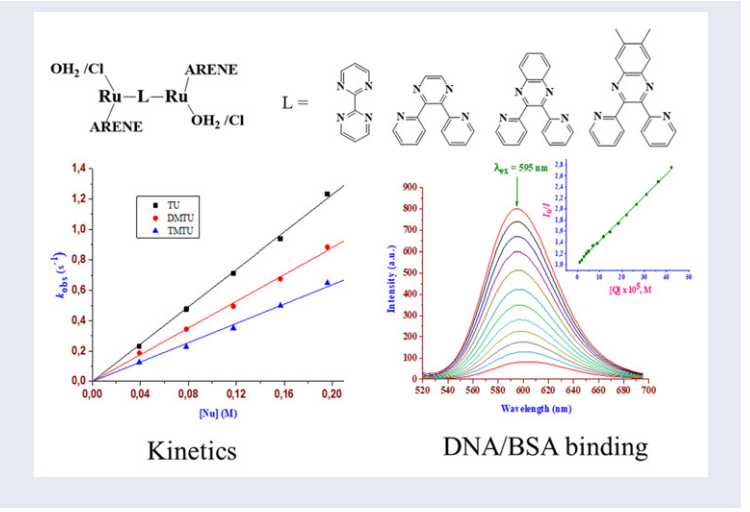

1. Introduction

Ruthenium complexes have been explored as an attractive alternative to platinum-based complexes as anticancer agents [1–3]. Their attractive properties include high cellular uptake, low systemic toxicity, and the ability to mimic iron in binding biomolecules [4]. Furthermore, they exist in numerous oxidation states under physiological conditions but commonly as ruthenium(II) or ruthenium(III) [2, 4].

The half-sandwich arene complexes form one of the most important classes of potential anticancer ruthenium(II) complexes [1]. They display a *pseudo*-octahedral geometry in which the π-bonded arene ligand occupies three coordination sites. The hydrophobic arene ligand facilitates diffusion of the drug through the cell membrane as well as stabilizes the metal center in its 2+ oxidation state. The other remaining three coordination sites offer diverse coordination modes that can be used to modulate the properties of the complexes [5].

Mononuclear (arene)Ru(II) complexes exhibit anticancer activities both *in vitro* and *in vivo* even in *cis*platin resistance cells. Their multinuclear analogues are more cytotoxic due to the possible synergistic effects of the bridging ligand at each metal center [1, 6–12]. The mechanism of antitumor action of Ru complexes is not well established but cytotoxicity is linked to their binding or interactions (covalently or non-covalently) with DNA and blood serum proteins (albumins and transferrin). Despite DNA and proteins being important macronucleophilic targets for the cytotoxicity by Ru complexes, their modes of binding have not been extensively studied [13–16].

Before reaching the said cytotoxic targets, metal-based drugs encounter an array of potential deactivators such as glutathione and cysteine residues of proteins. These macronucleophiles can competitively bio-transform the metallo-drugs depending on the kinetics and thermodynamics of the interactions, thereby influencing the equilibrium concentration of the drug in sera and intra-cellular fluids [17–19]. This can have an overbearing effect on the distribution and hence the anticancer activity of the drugs.

The nature, size, and electronic properties of the non-leaving ligands in the metal complexes influence the rate at which these interactions proceed. For instance, increasing the size of the polypridyl chelating ligand promotes cellular uptake, intercalation into the DNA double helix and the cytotoxicity of a complex [9, 20].

Reports are available on the interactions of *N,N*-chelated Ru complexes with DNA and bovine serum albumin (BSA) as well as their *in vitro* cytotoxicity with a variety of cell lines [21–25]. However, not much has been reported on the substitution behavior, DNA or BSA interactions and the cytotoxicity of homo- or hetero-bimetallic Ru complexes [11, 21]. Due to the foregoing reasons, we investigated the rate of substitution of aqua ligand(s) in a series (η^6-*p*-cymene)Ru(II) aqua complexes (**Ru1**–**Ru6**) using thiourea (Tu), *N,N*-dimethylthiourea (Dmtu) and *N,N,N′,N′*-tetramethylthiourea (Tmtu). Four of the complexes were binuclear with different π-conjugated ditopic *N,N*-chelate bridging ligands *viz*: 2,2′-bipyrimidine (**Ru3**), 2,3-*bis*(2-pyridyl)pyrazine (**Ru4**), 2,3-*bis*(2-pyridyl)quinoxaline (**Ru5**) and 6,7-dimethyl-2,3-*bis*(2-pyridyl)quinoxaline (**Ru6**). In addition, two mononuclear complexes, $[Ru(\eta^6\text{-}p\text{-cymene})(2,2'\text{-bipyridyl})OH_2)]^{2+}$ (**Ru2**) and $[Ru(\eta^6\text{-}p\text{-cymene})H_2O)_3]^{2+}$ (**Ru1**) were also studied for comparison. Aqua complexes were used because of the importance of hydrolysis of the metal-choro bond in anticancer mechanistic pathways [26]. Structures of the studied aqua(η^6-*p*-cymene)Ru(II) complexes are shown in Scheme 1.

In addition, binding interactions of **Ru7**–**Ru11** (chloro derivatives of **Ru2–Ru6**) with calf-thymus DNA (CT-DNA) and BSA was evaluated spectrophotometrically. Similar titrations could not be done for chloro derivative of **Ru1** because the salt only exists as the dimer from which the aqua solution (for kinetic analysis) was prepared *in situ*.

DFT computation of the lowest energy conformations and molecular docking studies were also performed to gain a further insight into the trend in the rate of substitution and binding studies, respectively.

2. Experimental

2.1. Materials and general procedures

All syntheses were performed under dinitrogen atmosphere using standard Schlenk techniques. Dichloro(η^6-*p*-cymene)Ru(II) dimer, 2,2′-bipyrimidine, 2,3-*bis*(2-pyridyl)pyrazine, 6,7-dimethyl-2,3-*bis*(2-pyridyl)quinoxaline, KPF_6, NH_4PF_6, 2,2′-bipyridyl, NaOH, $AgClO_4$, $NaClO_4{\cdot}H_2O$, $HClO_4$ (70 wt% solution), celite, Tu, Dmtu, Tmtu, CT-DNA, BSA, NaCl, tris(hydroxymethyl)amino methane hydrochloride (Tris-HCl) and 3,8-diamino-5-ethyl-6-phenylphenanthridinium bromide (EtBr) were supplied by Sigma-Aldrich. 2,3-*bis*(2-pyridyl)quinoxaline was synthesized according to literature method (Supplementary Information) [27]. Organic solvents were purchased from Merck (Pty) and used without further purification.

2.2. Synthesis of the (η^6-p-cymene) Ru(II) complexes

Triaqua(η^6-*p*-cymene)Ru(II) perchlorate (**Ru1**) and chloro Ru(II) complexes (**Ru7**–**Ru11**) were synthesized according to published literature methods [28–33].

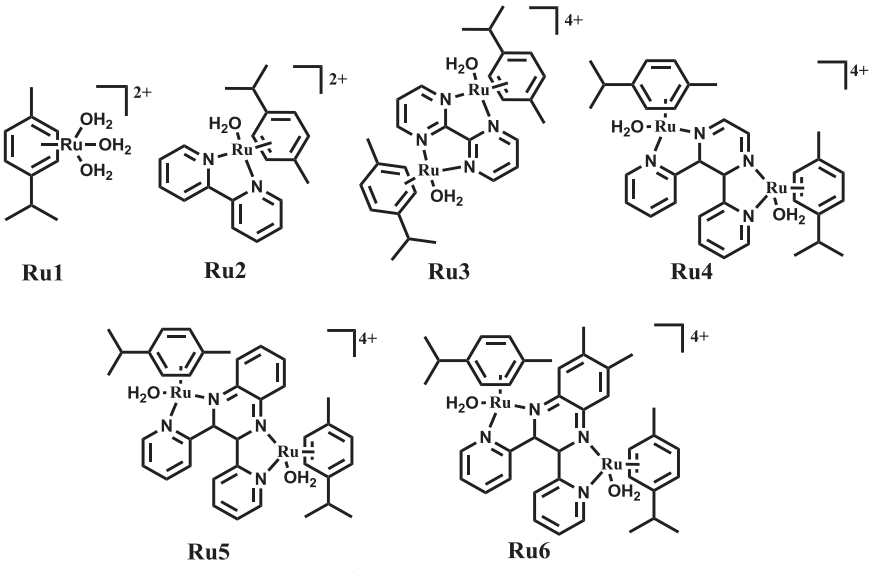

Scheme 1. Structures of cationic aqua(η^6-*p*-cymene)Ru(II) complexes (**Ru1**–**Ru6**).

2.2.1. Triaqua(η^6-p-cymene)Ru(II) perchlorate (Ru1)

The complex was synthesized *in situ* by reacting dichloro(η^6-*p*-cymene)Ru(II) dimer (100 mg, 0.16 mmol) with 3.99 equivalents of $AgClO_4$ in 0.01 M $HClO_4$ solution. The reaction mixture was stirred in the dark at 50 °C for 12 h. Upon cooling to room temperature, the solution was allowed to stand for 3 h and the grey AgCl precipitate therein was filtered off, and the filtrate was refrigerated at 4 °C before use.

2.2.2. Chloro(2,2′-bipyridyl)(η^6-p-cymene)Ru(II) hexaflourophosphate (Ru7)

A mixture of dichloro(η^6-*p*-cymene)Ru(II) dimer (100.0 mg, 0.16 mmol) and 2,2′-bipyridyl (59.0 mg, 0.38 mmol) in 25 mL of methanol was stirred at room temperature for 2 h. NH_4PF_6 (57.0 mg, 0.35 mmol) in 5 mL of methanol was added to the solution and the resulting mixture stirred for further 1 h. The orange-yellow precipitate which had formed was filtered off, washed with chilled methanol and diethyl ether. The product was further recrystallized by slow diffusion of diethyl ether into methanolic solution of the complex. Shiny yellow crystalline solids were obtained. Yield: (164.0 mg, 90%). Anal. Calcd for $C_{20}H_{22}ClN_2PF_6Ru$ (%): C, 42.0; H, 3.9; N, 4.9. Found: C, 42.3; H, 3.8; N, 4.7. ^{1}H NMR (400 MHz, acetone-d_6), δ (ppm): 9.62 (d, 2 H, $CH_{pyridyl}$), 8.62 (d, 2 H, $CH_{pyridyl}$), 8.32 (td, 2 H, $CH_{pyridyl}$), 7.82 (td, 2 H, $CH_{pyridyl}$), 6.25 (d, 2 H, $CH_{p\text{-}cymene}$), 6.00 (d, 2 H, $CH_{p\text{-}cymene}$), 2.67 (hept, 1 H, $CH_{p\text{-}cymene}$), 2.33 (s, 3 H, CH_3), 1.11 (d, 6 H, $CH(CH_3)_2$). ^{13}C NMR (400 MHz, acetone-d_6), δ (ppm): 155.8, 155.0, 140.0, 127.7, 123.8, 105.2, 104.0, 86.7, 84.5, 31.1, 27.7,18.1. MS (TOF, ESI^+), (*m/z*): 427.05 $[M]^+$.

2.2.3. Dichloro(μ_2-2,2′-bipyrimidyl)bis(η^6-p-cymene)diRu(II) bis(hexaflourophosphate) (Ru8)

A mixture of 122.0 mg (0.2 mmol) of the dichloro(η^6-*p*-cymene)Ru(II) dimer, 31.6 mg (0.2 mmol) of 2,2′-bipyrimidine and 77.0 mg (0.42 mmol) of KPF_6 in 20 mL methanol was stirred at room temperature for 4 h to form a yellow precipitate. The precipitate

was filtered off, washed with (3 × 10 mL) diethyl ether and dried under vacuum. Crystals of the complex were grown by slow diffusion of diethyl ether into an acetonic solution of the complex. Yield: (118.8 mg, 60%). Anal. Calcd for $C_{28}H_{34}Cl_2N_4P_2F_{12}Ru_2$ (%): C, 34.0; H, 3.5; N, 5.7. Found: C, 34.2; H, 3.8; N, 5.4. ^{1}H NMR (500 MHz, acetone-d_6), δ (ppm): 10.15 (d, 4 H, $CH_{pyridyl}$), 8.40 (t, 2 H, $CH_{pyridyl}$), 6.49 (d, 4 H, $CH_{p\text{-}cymene}$), 6.26 (d, 4 H, $CH_{p\text{-}cymene}$), 2.89 (hept, 2 H, $CH_{p\text{-}cymene}$), 2.36 (s, 6 H, CH_3) and 1.14 (d, 12 H, $CH(CH_3)_2$). ^{13}C NMR (500 MHz, acetone-d_6), δ (ppm): 163.8, 161.6, 126.9, 108.4, 105.2, 85.8, 84.1, 31.1, 21.5, 18.1. MS (TOF, ESI$^+$) (*m/z*): 429.05 [η^6-*p*-cymene RuCl-bipyrimidyl]$^+$, 270.99 [η^6-*p*-cymene-RuCl]$^+$.

2.2.4. Dichloro(μ$_2$-2,3-bis(2-pyridyl)pyrazine)bis(η^6-p-cymene)diRu(II) bis(tetrafluoroborate) (Ru9)

A mixture of dichloro(η^6-*p*-cymene)Ru(II) dimer (122.0 mg, 0.2 mmol) and 2,3-*bis*(2-pyridyl)-pyrazine (46.8 mg, 0.2 mmol) in 30 mL of methanol was stirred continuously at room temperature for 6 h. The solution was filtered through celite to remove any solid impurities. 10 mL of saturated methanolic solution of NH_4BF_4 was added to the filtrate and the resulting solution kept in a refrigerator for slow crystallization. After 2 days, a brown microcrystalline solid formed. It was filtered off, washed with methanol, diethyl ether and dried under vacuum. Yield: (129.7 mg, 67%). Anal. Calcd for $C_{34}H_{38}Cl_2N_4B_2F_8Ru_2$ (%): C, 43.0; H, 4.0 N, 5.9. Found: C, 42.8; H, 3.7; N, 6.0. ^{1}H NMR (400 MHz, DMSO-d_6), δ (ppm): 9.66 (m, 4 H, $CH_{pyridyl}$), 8.80 (s, 2 H, $CH_{pyrazine}$), 8.21 (t, 2 H, $CH_{pyridyl}$), 7.96 (t, 2 H, $CH_{pyridyl}$), 6.42 (m, 2 H, $CH_{p\text{-}cymene}$), 6.31 (d, 2 H, $CH_{p\text{-}cymene}$), 6.32 (br, 2 H, $CH_{p\text{-}cymene}$), 6.10 (d, 2 H, $CH_{p\text{-}cymene}$), 2.92 (hept, 2 H, $CH_{p\text{-}cymene}$), 2.31 (s, 6 H, $CH_{3p\text{-}cymene}$), 1.22 (dd, 12 H, $CH(CH_3)_2$). ^{13}C NMR (400 MHz, DMSO-d_6), δ (ppm): 158.1, 152.0, 140.7, 130.7, 130.5, 129.3, 109.8, 102.1, 88.1, 87.5, 87.4, 32.0, 22.5, 22.2, 18.5. MS (TOF, ESI$^+$) (*m/z*): 505.08 [(η^6-*p*-cymene)RuCl(2,3-*bis*(2-pyridyl)-pyrazine)]$^+$, 270.99 [η^6-*p*-cymene-RuCl]$^+$.

2.2.5. Dichloro(μ$_2$-2,3-bis(2-pyridyl)quinoxaline)bis(η^6-p-cymene)diRu(II) bis(hexafluorophosphate) (Ru10)

A mixture of 122.0 mg (0.2 mmol) of the dichloro(η^6-*p*-cymene)Ru(II) dimer, 56.8 mg (0.2 mmol) of 2,3-*bis*(2-pyridyl) quinoxaline and 77.0 mg (0.42 mmol) of NH_4PF_6 in 20 mL of methanol was refluxed for 4 h. After cooling to ambient temperature, the violet precipitate which had formed was filtered off, washed with (3 × 10 mL) water, 10 mL of methanol and 10 mL of diethyl ether and dried under vacuum. Dark violet shiny crystals were obtained. Yield: (185.1 mg, 83%). Anal. Calcd for $C_{38}H_{40}Cl_2N_4P_2F_{12}Ru_2$ (%): C, 40.9; H, 3.6; N, 5.0. Found: C, 41.1; H, 3.7; N, 4.8. ^{1}H NMR (500 MHz, DMSO-d_6), δ (ppm): 9.58 (d, 2 H, $CH_{pyridyl}$), 8.85 (m, 2 H, $CH_{pyridyl}$), 8.56 (d, 2 H, CH_{quinox}), 8.41 (m, 2 H), 8.24 (td, 2 H, $CH_{pyridyl}$), 8.01 (t, 2 H, CH_{quinox}), 6.43 (d, 2 H, $CH_{p\text{-}cymene}$) , 6.34 (d, 2 H, $CH_{p\text{-}cymene}$), 6.12 (m, 4 H, $CH_{p\text{-}cymene}$), 2.76 (hept, 2 H, $CH_{p\text{-}cymene}$), 2.51 (s, 6 H, CH_3), 1.15 (d, 6 H, $CH(CH_3)_2$), 1.02 (d, 6 H, $CH(CH_3)_2$). ^{13}C NMR (500 MHz, DMSO-d_6), δ (ppm): 157.7, 153.2, 149.9, 143.0, 140.4, 136.2, 131.6, 129.6, 129.2, 109.9, 102.7, 88.6, 87.4, 86.6, 84.1, 30.9, 22.6, 21.7, 18.0. MS (TOF, ESI$^+$) (*m/z*): 555.05 [(η^6-*p*-cymene)RuCl(2,3-*bis*(2-pyridyl)quinoxaline)]$^+$, 270.96 [η^6-*p*-cymene-RuCl]$^+$.

2.2.6. Dichloro(μ_2-6,7-dimethyl-2,3-bis(2-pyridyl)quinoxaline)bis(η^6-p-cymene)diRu(II) bis(hexaflourophosphate (Ru11)

A methanolic solution (30 mL) containing 122.0 mg (0.2 mmol) of dichloro(η^6-*p*-cymene)Ru(II) dimer, 62.4 mg (0.2 mmol) of 6,7-dimethyl-2,3-*bis*(2-pyridyl) quinoxaline and 77.0 mg (0.42 mmol) of KPF_6 was refluxed for 6 h. The resulting solution was concentrated to about 5 mL under reduced pressure and upon cooling excess diethyl ether was added to precipitate the complex. A deep brown precipitate was formed. This was filtered off, washed with (3 × 10 mL) of *n*-pentane and dried under vacuum. Yield: (160.0 mg, 70%). Anal. Calcd for $C_{40}H_{44}Cl_2N_4P_2F_{12}Ru_2$ (%): C, 42.0; H, 3.9; N, 4.9. Found: C, 41.8; H, 4.1; N, 4.7. ^{1}H NMR (400 MHz, acetone-d_6), δ (ppm): 9.57 (d, 2 H, $CH_{pyridyl}$), 8.57 (d, 2 H, $CH_{pyridyl}$) , 8.52 (s, 2 H, CH_{quinox}), 8.24 (t, 2 H, $CH_{pyridyl}$), 7.98 (t, 2 H, $CH_{pyridyl}$) 6.43 (d, 2 H, $CH_{pyridyl}$), 6.36 (d, 2 H, $CH_{p\text{-}cymene}$), 6.13-6.10 (m, 4 H, $CH_{p\text{-}cymene}$), 2.79-2.72 (m, 8 H, CH_{3quiox} and $CH_{p\text{-}cymene}$), 2.31 (s, 6 H, $CH_{3p\text{-}cymene}$), 1.30 (d, 6 H, $CH(CH_3)_2$), 1.18 (d, 6 H, $CH(CH_3)_2$). ^{13}C NMR (400 MHz, acetonitrile-d_3), δ (ppm): 157.2, 153.1, 148.8, 142.5, 140.2, 129.8, 129.1, 110.5, 102.1, 88.8, 87.6, 85.8, 83.5, 48.9, 31.0, 29.9, 21.7, 21.0, 20.3, 17.4. MS (TOF, ESI$^+$) (*m/z*): 583.13 [(η^6-*p*-cymene)RuCl(6,7-dimethyl-2,3-*bis*(2-pyridyl)quinoxaline)]$^+$, 270.99 [η^6-*p*-cymene-RuCl]$^+$.

2.3. Physical measurements and instrumentation

NMR spectra were acquired on a Bruker Avance DPX III 400/500 MHz spectrometer fitted with a 5-mm probe at 303 K. NMR chemical shifts (δ, ppm) were referenced to those of $Si(CH_3)_4$. Mass spectra were recorded on a Premium Micromass (TOF, ESI$^+$) spectrometer. NMR and MS spectra are presented in the Supplementary Information (Figures S1–S18). Microanalyses (C, H, and N) of the complexes were carried out on a Thermo Scientific Flash 2000 analyzer. A Cary 100 Series UV-vis spectrophotometer thermostrated by a Cary temperature controller (± 0.05 °C) was used for acid-base pH titrations, kinetic measurements and CT-DNA titrations. Observed rate constants for the reactions of **Ru1** were measured on an Applied Photophysics SX 20 stopped-flow reaction analyzer equipped with an online data acquisition program. The temperature of the analyzer was maintained within ± 0.1 °C. Fluorescence emission spectra were recorded using a Perkin Elmer LS 45 Fluorescence Spectrometer. pH of the aqueous solutions of the complexes was determined by a Jenway 4330 pH meter with an attached glass microelectrode (4.5 mm) filled with a 3.0 M NaCl solution. The pH meter was calibrated with standard buffer solutions (pH 4.0, 7.0, and 10.0) before use. p*K*a and kinetic data were fitted to standard non-linear equations using OriginPro 9.1® program [34].

2.4. Aquation of the complexes

Aqua complexes **Ru2**–**Ru6** were prepared by reacting a known amount of the chloro complexes **Ru7**–**Ru11** with slightly less stoichiometric amounts of $AgClO_4$ in 0.01 M $HClO_4$ solution to ensure that the aqua complexes were not contaminated with Ag^+ ions. All the reactions were carried out in the dark at 50 °C for 48 h after which the

AgCl precipitate, which had formed, was filtered off using a Millipore filtration system [35]. The filtrates were refrigerated at 4 °C before use.

2.5. pKa determination

Spectrophotometric acid–base titration of the aqua complexes with NaOH was done from pH 1–12 at 298 K. To avoid dilution effects and absorbance corrections, large volumes of the complexes (about 500 mL) were used [36]. From pH 1–3, small granules of crushed NaOH pellets were added stepwise while from pH 4–12, NaOH solutions of decreasing concentrations were added dropwise. After each addition, the mixture was stirred for about 2 min prior to pH and spectral recording. About 0.6 mL of the solution was used for pH measurements and discarded to avoid *in situ* contamination of the stock complex solution by Cl^- ions from the meter. The aliquots for absorbance measurements were returned to the stock solution. A confirmatory reverse pH titration was done using $HClO_4$ solutions in place of NaOH.

2.6. Kinetic measurements

The aqua complexes and nucleophile solutions were maintained at pH 2.0 and ionic strength of 0.1 M $HClO_4/NaClO_4$. The concentration of the aqua complexes were **Ru1** (1.307 mM), **Ru2** (0.440 mM), **Ru3** (0.430 mM), **Ru4** (0.103 mM), **Ru5** (0.561 mM), and **Ru6** (0.525 mM). Substitution studies were done under *pseudo*-first order conditions in which the concentration of the nucleophile was at least 10 folds higher with respect to the concentration of each leaving group in the complex. UV-Vis spectral changes of the reactions were taken to determine appropriate wavelength to follow each reaction, which was then done by monitoring absorbance changes as a function of time at the specific wavelength. Concentration dependence studies were performed at 25 °C while the temperature dependence reactions were studied from 20 to 40 °C at an interval of 5 °C. The results recorded herein are an average of three independent runs.

2.7. DNA binding studies

2.7.1. Absorption spectral studies

CT-DNA binding experiments were performed at room temperature in 5 mM Tris-HCl/50 mM NaCl buffer (pH = 7.4) solution. A stock solution of the complex (5 mM) was prepared in 50% DMSO. The concentration of the CT-DNA was determined from a Beer-Lambert plot by measuring the absorption intensity at 260 nm, where the molar absorptivity of CT-DNA is about 6600 $M^{-1}cm^{-1}$. The absorbance ratio at 260 and 280 nm (A_{260}/A_{280}) was measured and found to be in the range of 1.8–1.9, indicating that the DNA was sufficiently free of protein [37].

A fixed concentration (20 μM) of each complex (**Ru7–Ru11**) was titrated spectrophotometrically with increasing CT-DNA concentration (0–20 μM). The absorption spectra were obtained by adding the requisite amount of CT-DNA to both the reference and sample solutions to eliminate the absorbance of the CT-DNA. The Ru(II) complex-DNA solutions were allowed to incubate for 10 min in quartz cuvettes prior to

absorption spectra recording. The absorption changes were monitored at the metal-to-ligand charge transfer (MLCT) bands of the complexes as a function of the concentration of CT-DNA. The binding affinities of the Ru(II) complexes were calculated using the Wolfe-Shimer equation [38] *i.e.*, $[CT\text{-}DNA]/(\varepsilon_a-\varepsilon_f) = [CT\text{-}DNA]/(\varepsilon_b-\varepsilon_f) + 1/(K_b(\varepsilon_b-\varepsilon_f))$, where [CT-DNA] is the concentration of CT-DNA, and ε_a, ε_f, and ε_b are the molar absorptivity of titrated mixture (A_{obs}/[complex]), unbound Ru complex and the (Ru complex-CT-DNA) complex, respectively. K_b (intrinsic binding constant) was calculated from the ratio of the slope to the intercept of the plot of $[DNA]/(\varepsilon_a-\varepsilon_f)$ *versus* [DNA].

2.7.2. Fluorescence spectral studies

The fluorescence quenching experiments were performed using EtBr to probe the competitive binding abilities of the Ru(II) complexes on the CT-DNA. Fixed concentration of EtBr-CT-DNA (10 μM each of CT-DNA and EtBr) was prepared in 5 mM Tris-HCl/50 mM NaCl buffer (pH = 7.4) solution. The competitive binding effects of **Ru7**–**Ru11** on the EtBr-CT-DNA complex was monitored by adding aliquot amounts of the stock Ru(II) complexes solutions in incremental amounts to EtBr-CT-DNA solutions. The excitation of the solutions was done at 500 nm and changes in fluorescence emission were recorded within the wavelength range of 520–700 nm. Before recording the spectra, the solutions were thoroughly mixed and incubated for 10 min at room temperature. The quenching efficiency of the complexes was analyzed using the Stern-Volmer equation [39] *i.e.*, $I_o/I = 1 + K_{sv}[Q] = 1 + k_q\tau_0$, where I_o and I are the emission intensities of EtBr-CT-DNA complex in the absence of the complex and after each addition of complex, respectively, while [Q] is the concentration of quencher (Ru(II) complex). The Stern-Volmer (quenching) constant, K_{sv}, was determined from the slope of the linear plot of I_o/I *versus* [Q]. To have an insight on the kinetics of the competitive binding process, the bimolecular quenching rate constants, k_q, were also computed using the Stern-Volmer equation, where τ_0 is the average fluorescence lifetime of the EtBr-CT-DNA complex in the absence of the quencher (23 ns at room temperature) [40]. The apparent binding constant, K_{app}, was computed from the equation $K_{EtBr}[EtBr] = K_{app}[Q]$, where [Q] is the concentration of quencher causing 50% reduction in fluorescence intensity of EtBr-CT-DNA complex, $K_{EtBr} = 1.0 \times 10^7\ M^{-1}$ [41] and [EtBr] was taken as 50 μM. The binding constant, K_F, was determined using the Scatchard equation $\log(I_o - I)/I = \log K_F + n\log[Q]$, where n is the number of binding sites per nucleotide.

2.7.3. BSA-binding studies

Quenching of the fluorescence emission of BSA by **Ru7**–**Ru11** was performed to determine their binding constants on the protein. The concentration of BSA was measured spectrophotometrically using the Beer-Lambert formulation where a ε_{max} value of $4.4 \times 10^4\ M^{-1}cm^{-1}$ at 278 nm (λ_{max}) was used [42]. Stock concentration of BSA (10.4 μM) was prepared in 5 mM Tris-HCl/50 mM NaCl buffer solution at a pH of 7.4. The emission spectra of equilibrated 30 μM of the buffered BSA solutions in the absence and presence of the complexes of concentration ranging from 0 to 130 μM were acquired at room temperature. The emission changes were recorded in the λ_{em} range of 250–450 nm, with the

excitation wavelength set at 278 nm for all binding interactions. Each spectrum was recorded after an incubation period of 10 min. The quenching efficiency of the complexes was calculated using the Stern-Volmer and Scatchard equations as discussed above.

To investigate primary and secondary inner-filter effects (IFE), we measured the spectral data of each chloro complex at the concentration used for the titration (20 μM) and compared them with those recorded during the titration with CT-DNA and BSA at their excitation/emission wavelengths (510/596 nm for CT-DNA and 278/348 nm for BSA titrations, respectively). The absorbance of all the complexes are lower than 0.2 at these wavelengths (Figure S26). Literature reports that IFE corrections are necessary only if the absorbance of the fluorophore exceed 0.3 [43, 44]. At the low concentration used (20 μM), self or re-absorption of the fluorescence is appreciably low to warrant any corrections. Thus, no further effort was made to correct the fluorescence readings for the titration data.

2.8. Quantum chemical calculations and molecular dockings

Computation of lowest energy conformations of the aqua complexes **Ru1**–**Ru6** was performed using the Gaussian 09W suite of programs. Visualization was done in GaussView 5.0 program [45]. Density functional theory (DFT) was applied to optimize the structures using the hybrid B3LYP method employing the Los Alamos National Laboratory 2-double-z effective core potential [46]. To account for solvent effects, optimization was simulated in aqua environment using conductor-like polarizable continuum solvent model. Formal charges of +4 and +2 were assigned to the binuclear and mononuclear complexes, respectively. Global electrophilicity indices (ω) for the complexes were calculated from the relationship, $\omega = \mu^2/2\eta$ [47]. Natural Bond Order (NBO) analysis was used to determine atomic charges of each atom in these complexes [45]. The complexes were optimized at singlet spin ground electronic state.

The chloro complexes **Ru7**–**Ru11** were docked onto B-DNA using HEX8.0 software [48]. The coordinates of all the complexes were optimized by Gaussian 09 program and converted to protein data bank (PDB) format using Mercury 3.3 software [49]. The crystal structure of the B–DNA dodecamer $d(CGCGAATTCGCG)_2$ (PDB ID: 1BNA) was retrieved from the protein data bank [50]. The docked pose of 1BNA and each complex were viewed using CHIMERA software [51]. The docking protocol was repeated three times and almost similar docking poses were viewed in each of the runs. The $E_{(\text{lowest energy pose})}$ value of each Ru complex and DNA interactional pose was evaluated.

3. Results and discussion

3.1. Acid-base equilibrium of the aqua complexes

The p*K*a values of the aqua complexes were determined by fitting a single or a double Boltzmann standard equation on the plot of absorbance versus pH at a selected wavelength. Typical absorption spectra are shown in Figure 1 for the titration of **Ru6** with NaOH. The inset shows complementary plots of absorbance versus pH at $\lambda = 270$ and

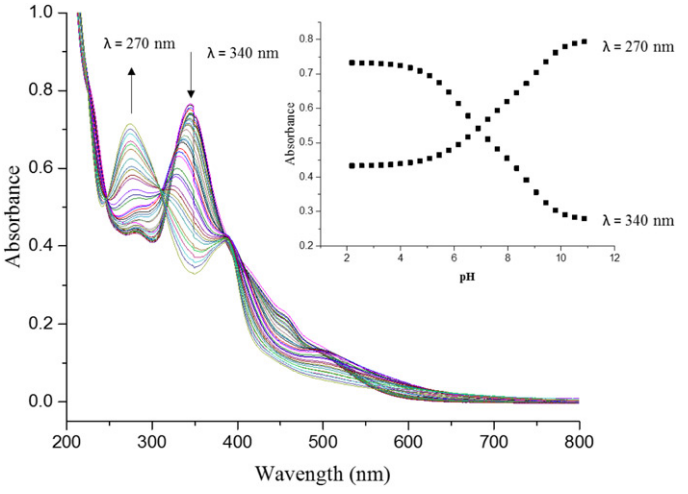

Figure 1. UV-vis spectral changes for **Ru6** as a function of pH. Inset: Plots of absorbance *versus* pH at $\lambda = 270$ and 340 nm.

Table 1. pKa values obtained for the deprotonation of the complexes.

Complex	Ru1	Ru2	Ru3	Ru4	Ru5	Ru6
p*Ka*$_1$	4.21 ± 0.01	7.38 ± 0.02	6.12 ± 0.05	6.29 ± 0.08	6.02 ± 0.02	6.32 ± 0.03
p*Ka*$_2$	–	–	8.21 ± 0.21	8.50 ± 0.23	8.15 ± 0.32	8.91 ± 0.10

340 nm. Additional spectra are presented in Figures S19 and S20 while the p*K*a values are summarized in Table 1.

From the data in Table 1, the aqua ligands in **Ru1** are the most acidic, since the complex has the lowest p*K*a value in the series [52]. The p*K*a value of **Ru2** is by 1 pH unit higher than p*Ka*$_1$ of its related binuclear congener **Ru3**, showing that the aqua ligands in **Ru3** are more acidic due to increased positive charge as well as the added effects of increased π-back-bonding of electron density from the metal centers [53]. The p*K*a values decrease with increase in the strength of π-acceptor ability of the bridging ligand [36, 54]. An increase in π-acceptor enhances the withdrawal of electrons from the metal center, thus making the aqua ligands more acidic [26]. The stepwise deprotonation of the aqua ligands in the binuclear complexes **Ru3**–**Ru6** is presented in Scheme 2. It was observed that the p*Ka*$_2$ values in the binuclear complexes are at least 2 p*K*a units higher than their respective p*Ka*$_1$. This is because upon deprotonation of the first aqua ligand, the overall charge of the complex reduces from +4 to +3 making the second Ru metal center less electrophilic, thereby decreasing the tendency for another deprotonation to occur [53, 55, 56]. The methyl groups of the quinoxaline moiety in **Ru6** lower the electrophilicity of the complex by increasing the electronic density at the metal center through σ-inductive effects. Hence, its aqua ligands are the least acidic.

The p*K*a value of **Ru1** (4.21) is similar to what has been reported for other mononuclear (arene)Ru(II)(aqua) complexes, where deprotonation of the coordinated aqua ligand only commences when solutions have pH values above 3.0 [33, 57]. Data presented in Table 1 indicates that the aqua complexes are quite stable below pH 3.0. It can be hypothesized that in hypoxia media (associated with hyper growth of the

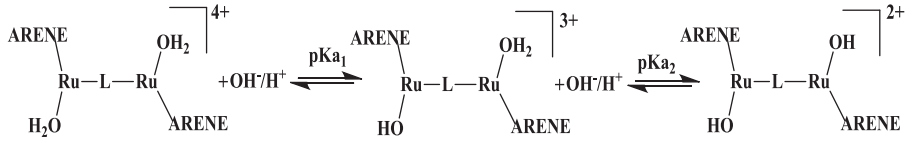

Scheme 2. Stepwise deprotonation of the aqua ligands in the binuclear complexes **Ru2**–**Ru6**.

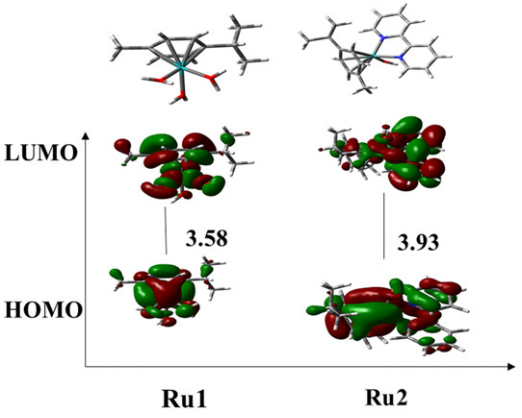

Figure 2. DFT-optimized frontier molecular orbitals of the mononuclear aqua complexes.

cancer cells), the chloro(η^6-*p*-cymene)Ru(II) derivatives are activated into various Ru-H_2O/OH (for mono) and HO-/H_2O-Ru-L-Ru-Cl or HO-/H_2O-Ru-L-Ru-OH_2/-HO species (for binuclear) in relative proportions that depend on the pH and the stability of the hydrolysis intermediates. This was the case with *in vitro* activation of the chloro(RAPTA)Ru (mono, bi and poly metallic) complexes [58], which resulted in the formation of reactive aqua Ru species at pH lower than 3.0. To ensure that our kinetics bear this relevance, we maintained a pH of 2.0 for all the substitution reactions.

3.2. Computational studies

Computed data of the lowest energy conformations of the Ru complexes are helpful in explaining the observed substitution reactivity trends. Figures 2 and 3 show the DFT-optimized structures of the frontier molecular orbitals and their respective energy separation. Key computational data derived from the structures are summarized in Table 2. The complexes adopt a *pseudo*-octahedral geometry in which the *p*-cymene moiety is located opposite the aqua ligand to minimize steric interactions [28]. In **Ru3-Ru6**, the two aqua ligands are *trans* to each other. In **Ru3**, the two pyrimidinyl moieties are co-planar because the bridging ligand coordinates each metal center through two equivalent nitrogen atoms. However, in the rest of the binuclear complexes, the bridging ligand coordinates the metal centers through non-equivalent nitrogen atoms; a pyridyl and pyrazinic/quinoxalinic. The two pyridyl moieties in these binuclear complexes are not co-planar to each other. This occurs in order to ameliorate the steric interactions of the hydrogen atoms at the *meta* positions in the pyridyl rings [59, 60]. The angle between the two pyridyl moieties in **Ru4**, **Ru5**, and **Ru6** is 50.68°, 56.33°, and 55.54°, respectively. Figure 4 illustrates the non-planarity of the pyridyl moieties in **Ru4**.

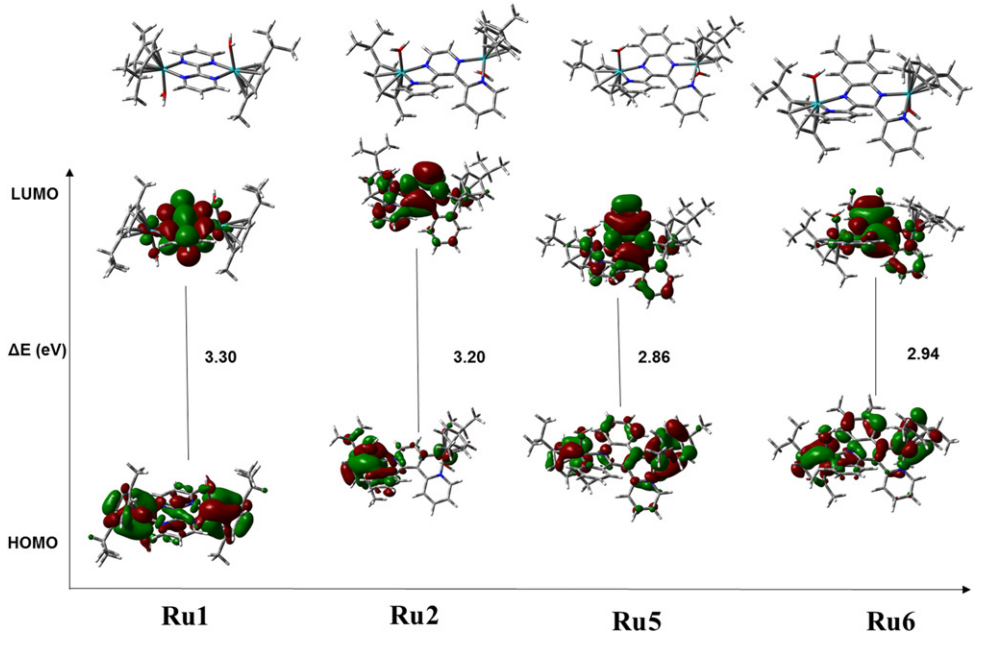

Figure 3. DFT-optimized frontier molecular orbitals of the binuclear aqua Ru(II) complexes.

Table 2. Summary of selected computational data for complexes.

Complex		Ru1	Ru2	Ru3	Ru4	Ru5	Ru6
HOMO-LUMO energy							
HOMO/eV		−6.62	−6.98	−7.57	−7.18	−7.18	−7.12
LUMO/eV		−3.04	−3.05	−4.27	−3.98	−4.32	−4.18
HOMO-LUMO gap/eV		3.58	3.93	3.30	3.20	2.86	2.94
NBO charges	Ru_1	0.383	0.280	0.306	0.303	0.284	0.281
	Ru_2	–	–	0.306	0.303	0.284	0.281
Electrophilicity index (ω)/eV		6.52	6.40	10.62	9.73	11.52	10.86
Dipole moment/D		8.69	4.89	0.003	5.08	6.77	8.43
Ru-OH_2 bond length/Å		2.254	2.154	2.151	2.158	2.144	2.153
Ru-Ru distance/Å		–	–	5.66	6.88	6.95	6.96
Pyridyl Inter-planar angle/°		–	–	–	50.68	56.33	55.54

In the chelated complexes, the HOMO is largely based on the metal center(s) and *p*-cymene group(s) while the LUMO is largely based on the chelating ligand. The binuclear complexes have a smaller energy gap compared to the mononuclear complexes because the second metal center stabilizes the π^* orbitals of the ligand by lowering the HOMO–LUMO gap [61, 62]. The energy levels of the dπ HOMO of the **Ru4**, **Ru5**, and **Ru6** is invariant as the bridging ligand is systematically varied. Thus, the bridging ligand has little effect on the relative energy of dπ HOMO. On the contrary, the π^* LUMO energy is somewhat affected by the bridging ligand.

3.3. Kinetics studies

The substitution of the aqua ligand(s) in **Ru1**–**Ru6** by thiourea nucleophiles of varied steric demands under *pseudo*-first order conditions showed a single substitution step. Representative spectral changes for the reactions of **Ru2** (mononuclear) and **Ru5**

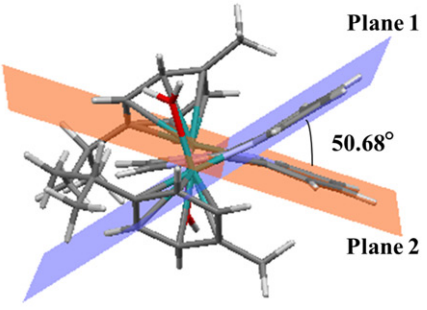

Figure 4. DFT-optimized diagram of **Ru4** showing the inter-planar angle between its pyridyl moieties.

(binuclear) with Dmtu are shown Figures 5 and 6, respectively. Kinetic traces taken at a suitable wavelength were fitted into single exponential standard function. The least-square fit to the exponential function gave the *pseudo*-first order rate constants (k_{obs}) which were then plotted against nucleophile concentrations. k_{obs} values are presented in the Supplementary Information (Tables S1–S6). All the plots had a linear dependence of k_{obs} on the nucleophilic concentration with zero intercepts as shown in Figure 7 and Figures S21 and S22. The slopes of the plots gave the second order rate constants (k_2). Therefore, the rate of reaction can be described by equation: $k_{obs} = k_2$[Nucleophile]. The k_2 values obtained are summarized in Table 3.

Activation parameters were calculated from Eyring plots (ln(k_2/T) versus T^{-1}) and the values obtained are also tabulated in Table 3. Typical Eyring plots are presented in Figure 8 while the ln(k_2/T) and respective T^{-1} values are given in Tables S7–S12. Additional Eyring plots are presented in Figures S23 and S24. For all the studied complexes, the activation enthalpies ($\Delta H^{\neq}$) are positive while the activation entropies ($\Delta S^{\neq}$) were negative.

The rate of aqua substitution from the complexes bridged by varied N,N-aromatic chelate bridge (**Ru3**–**Ru6**) was measured. Also included for comparison purposes are two mononuclear complexes **Ru1** and **Ru2**. In **Ru1**, the Ru(II) metal center is bonded to *p*-cymene and three aqua ligands. In **Ru2**, two aqua ligands in **Ru1** were replaced by a bidentate 2,2′-bipyridyl chelating ligand. In this discussion, the reactivity of the complexes with Tu is used as a representative.

Data in Table 3 show that the k_2 values for the simultaneous substitution of the aqua ligands in the binuclear complexes decreased in the order **Ru3** > **Ru4** > **Ru5** > **Ru6**, in line with the stereo-electronic effects of the *N,N*-aromatic bridging ligand. Due to the symmetric A-A ditopicity of the bridging ligand in **Ru3**, the space around the metal centers is less restricted compared to the A-B ditopic bridging ligand in the other binuclear complexes. As a result, the approaching nucleophile faces less steric hindrance towards the metal centers in **Ru3** compared to the other binuclear complexes. The comparative magnitude of the global electrophilicity indices indicates that **Ru3** is more electrophilic than **Ru4**. This is also corroborated by the relative magnitude of the Ru NBO charges of 0.306 (**Ru3**) and 0.303 (**Ru4**). The higher reactivity of **Ru3** compared to **Ru4** is also attributable to the fact that the 2,2′-bipyrimidine bridging ligand is a stronger π-acceptor than 2,3-*bis*(2-pyridyl)pyrazine. The two nitrogen

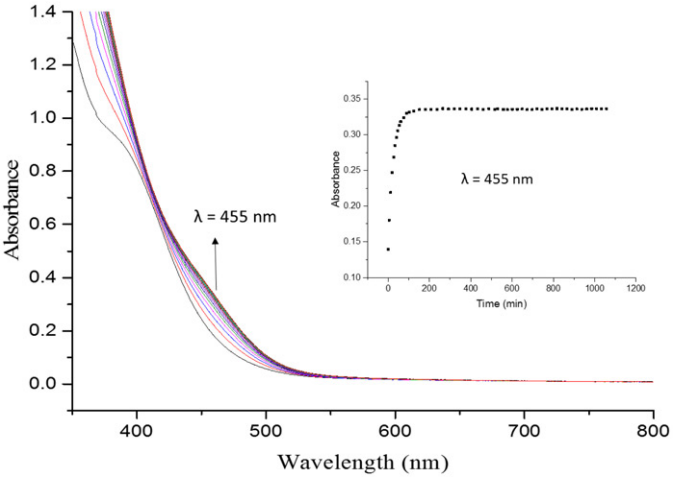

Figure 5. UV-vis spectra for the reaction of **Ru2** with Dmtu at 298 K, pH = 2.0, $I = 0.1$ M $HClO_4$/$NaClO_4$. Inset: Kinetic trace taken at $\lambda = 455$ nm.

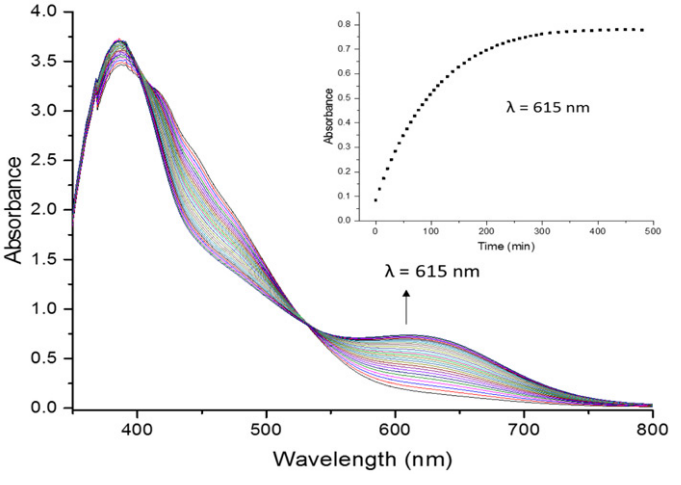

Figure 6. UV-vis spectra for the reaction of **Ru5** with Dmtu at 298 K, pH = 2.0, $I = 0.1$ M $HClO_4$/$NaClO_4$. Inset: Kinetic trace taken at $\lambda = 615$ nm.

atoms of each pyrimidine moiety of 2,2′-bipyrimidine bridge are *meta*-positioned making the bridge a better π-acceptor than 2,3-*bis*(2-pyridyl)pyrazine in which the pyrazinic N atoms are *para*-positioned causing a more effective σ-overlap of its orbitals with the metal, making it a better σ-donor bridge [63]. This electron-donating effect makes the ligand a less effective π-acceptor compared to the former bridging ligand [64]. In **Ru5**, the additional fused ring enhances the π-acceptor character of the A-B ditopic bridging ligand, as a result of stabilized π^* LUMOs leading to decreased HOMO-LUMO gap [65, 66]. Thus, π-back donation of electron density from the metal center to the bridging ligand of **Ru5** is energetically favored, making the complex more electrophilic. This is supported by the trend in the magnitude of the calculated global electrophilicity index (Table 2). However, the reactivity of **Ru5** is out of

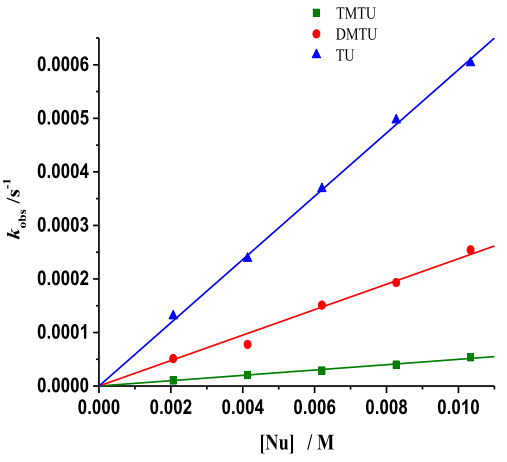

Figure 7. Plots of k_{obs} *versus* concentration of thiourea nucleophiles for the substitution of the aqua ligands in **Ru4** at 298 K, pH = 2.0, $I = 0.1$ M $HClO_4/NaClO_4$.

Table 3. Values of k_2, $\Delta H^{\neq}$, and $\Delta S^{\neq}$ for the substitution of the aqua ligands from **Ru1–Ru6** by thiourea nucleophiles.

Complex	Nu	k_2 (10^{-2} M^{-1}s^{-1})	$\Delta H^{\neq}$ (kJmol^{-1})	$\Delta S^{\neq}$ (Jmol^{-1} K^{-1})
Ru1	**Tu**	614 ± 7	62 ± 2	−23 ± 7
	Dmtu	440 ± 6	65 ± 2	−17 ± 6
	Tmtu	319 ± 7	67 ± 2	−13 ± 7
Ru2	**Tu**	7.77 ± 0.09	63 ± 3	−56 ± 10
	Dmtu	6.26 ± 0.10	57 ± 2	−77 ± 6
	Tmtu	2.10 ± 0.04	68 ± 1	−47 ± 4
Ru3	**Tu**	28.71 ± 0.30	56 ± 2	−71 ± 7
	Dmtu	13.53 ± 0.30	63 ± 3	−51 ± 9
	Tmtu	1.28 ± 0.02	76 ± 2	−25 ± 8
Ru4	**Tu**	5.91 ± 0.05	57 ± 2	−77 ± 7
	Dmtu	2.38 ± 0.08	67 ± 2	−51 ± 8
	Tmtu	0.50 ± 0.01	76 ± 3	−33 ± 9
Ru5	**Tu**	0.17 ± 0.01	80 ± 2	−29 ± 7
	Dmtu	0.14 ± 0.01	83 ± 2	−22 ± 5
	Tmtu	0.09 ± 0.02	87 ± 2	−11 ± 6
Ru6	**Tu**	0.12 ± 0.01	84 ± 2	−20 ± 6
	Dmtu	0.11 ± 0.01	84 ± 2	−19 ± 7
	Tmtu	0.05 ± 0.07	88 ± 2	−18 ± 6

sequence based on the trend of the electrophilicity index and a smaller energy gap in its frontier orbitals. This can be accounted for by an increase in steric hindrance around its metal centers as shown by the largest inter-plane angle of 56.33° (Table 2) between its pyridyl rings. In addition, the localized charge on the metal centers is less positive, due to the strong σ-donation by the 2,3-*bis*(2-pyridyl)quinoxaline bridging ligand.

The two methyl substituents in the 2,3-*bis*(2-pyridyl)quinoxaline framework in **Ru6** enhances σ-donation towards the metal centers. The LUMOs assume higher energies leading to a widening of the energy gap, which decreases π-back-bonding of electron density into the π-orbitals of the bridging ligand. Thus, electron density from the methyl substituents in the chelating bridge of **Ru6** accumulates at the metal centers leading to decreased reactivity. In support of this argument, is an observation that the

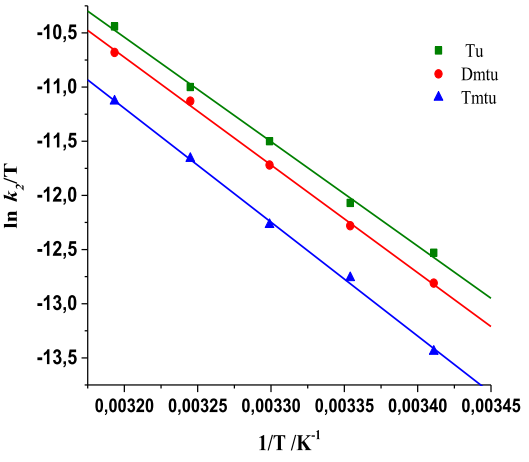

Figure 8. Eyring plots for the reaction of **Ru5** with different thiourea nucleophiles, pH = 2.0, $I = 0.1$ M $HClO_4/NaClO_4$.

presence of methyl substituents in 2,3-*bis*(2-pyridyl)quinoxaline framework shifts the reduction potential of free ligand to a more negative value compared to the unsubstituted 2,3-*bis*(2-pyridyl)quinoxaline [61]. Therefore, the slower rates of substitution from both **Ru5** and **Ru6** in comparison to **Ru4** is due to both steric and σ-donation effects.

The DFT calculated data for Ru–Ru separation distance of the complexes (Table 2) exhibit an inverse correlation with the reactivity observed trend. As the inter-metallic Ru-Ru distance increases from **Ru3** to **Ru6**, the delocalization of electron density within the bridging ligand decreases leading to the reduced synergy between the metal centers thus lowering the reactivity [67]. An inverse relationship also exists between the calculated dipole moments (a measure of the inductive negative charge of a system [68]) and the reactivity of the binuclear complexes. The positive charge at the Ru metal centers decreases from **Ru3** to **Ru6** as shown by the Ru NBO charges. A decreasing trend of the Ru charge and hence the dipole of the complexes is reflected in the lower rate of substitutions of the aqua ligands from the complexes.

Ru3 is ten times more reactive than its closely related mononuclear analogue **Ru2** because its 2,2,-bipyrimidine ligand is a stronger π-acceptor than the 2,2′-bipyridyl ligand in **Ru2** [63, 64]. Thus, the metal centers in **Ru3** are more susceptible to nucleophilic attack. Also important are the synergistic electronic effects on each metal center conveyed through the π-system of the *bis*-chelated 2,2′-bipyrimidine bridging ligand [28]. These factors stabilize the energy of the LUMO in **Ru3** leading to a narrower frontier orbital energy gap [61, 62]. As a consequence, **Ru3** is more electrophilic, due to decreased electron density at the metal center as evidenced by the large magnitude of the Ru NBO charge (Table 2). This is also corroborated by the lower pKa_1 value of 6.12 (**Ru3**) compared to that of **Ru2** (7.38).

Ru1 is found to be $\sim 10^2$ folds more reactive than **Ru2**. The computed global electrophilicity index is higher for **Ru1** than **Ru2** implying that the former complex is more electrophilic. This is supported by the low p*K*a value and higher NBO charge on the Ru metal center in **Ru1** compared to **Ru2**. Therefore, the metal center in **Ru1** is more electron-deficient and thus more attractive for the facile nucleophilic attack. The

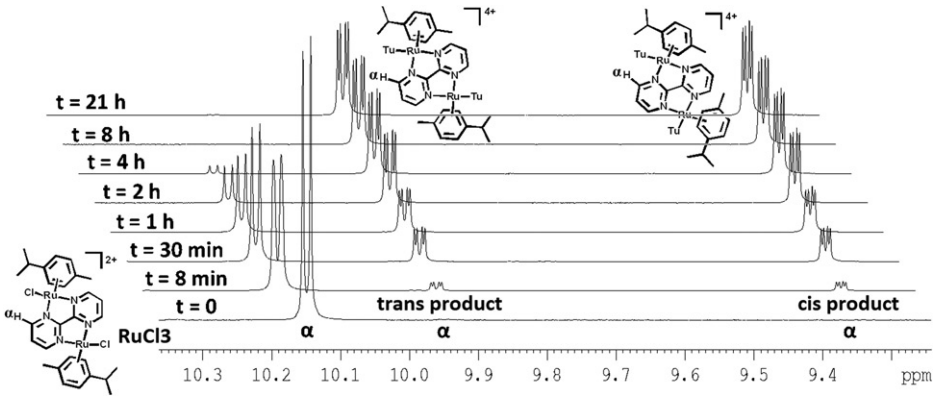

Figure 9. ^{1}H NMR spectral array obtained for the reaction of **Ru8** with Tu (6 equivalents) in acetone-d_6 at 303 K.

reactivity of **Ru1** is further enhanced by the significantly weaker Ru-OH_2 bond compared to **Ru2**. This is evidenced by the Ru-OH_2 bond lengths of 2.254 Å (**Ru1**) and 2.154 Å (**Ru2**). Thus, the aqua ligand of **Ru2** is more strongly bonded and therefore less labile [69]. Furthermore, the 2,2′-bipyridyl chelating ligand in **Ru2** introduces steric hindrance around the metal center, thereby impeding nucleophilic attack. In the same manner, the bipyridyl ligand in [η^6-benzene Ru(H_2O)(bipyridyl)]$^{2+}$ was found to retard the rate of water exchange by 100 folds compared to that of [η^6-benzene Ru(H_2O)$_3$]$^{2+}$ [70].

The reactivity of the three nucleophiles follow the order Tu > Dmtu > Tmtu according to the steric bulkiness of the nucleophile. As the bulkiness increases, the approach towards the metal center is retarded causing transition state destabilization, hence slowing down the reactivity [71]. The negative values for $\Delta S^{\neq}$ obtained suggest an associatively activated substitution process dominated by bond-making with the incoming nucleophile. The negative activation entropy also implies a more ordered transition state compared to the starting reactants and the final products [72, 73].

3.4. ^{1}H NMR kinetics studies

To gain further insight into the substitution process of the binuclear complexes, a reaction of the chloro complex **Ru8** (a binuclear with a symmetric and ditopic 2,2′-bypyrimidyl *N,N*-chelate bridge) with six equivalents of Tu was monitored by ^{1}H NMR in acetone-d_6 at 303 K. An overlay of the time dependent spectra obtained is shown in Figure 9. To effectively monitor the reaction, an aromatic proton (H_α) adjacent to the pyrimidinic N was chosen since it is the closest to the coordinated N atom and thus would be the most likely affected by perturbations of electron density in and around the metal center during the substitution reaction. The proton H_a for unreacted **Ru8** resonated at $\delta = 10.14$ ppm and on reaction with Tu, its resonance peak shifted slightly downfield to 10.16 ppm. The intensity of this peak decreased progressively over time. As the reaction progressed, a new set of two peaks emerged (~8 min) at $\delta = 9.92$ ppm (due to *trans*-isomer) and $\delta = 9.34$ ppm (due to *cis*-isomer product) appeared. These peaks gradually increased in intensity maintaining an equal isomeric

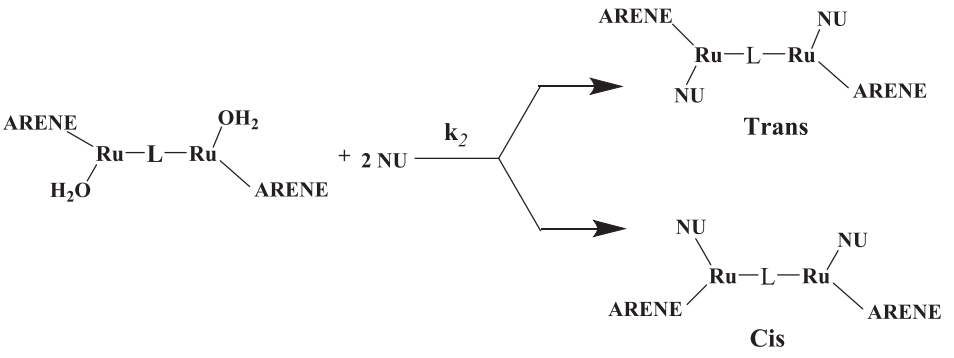

Scheme 3. Proposed reaction pathway for the binuclear aqua complexes.

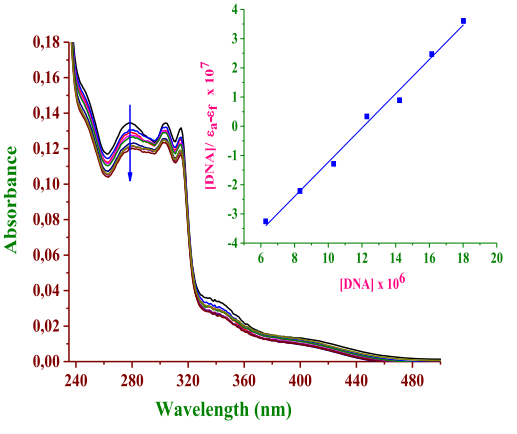

Figure 10. UV-vis absorption spectra of **Ru7** (20 μM) with increasing [CT-DNA] (0-20 μM). The arrow indicates a decrease in absorbance with increase in [CT-DNA]. Inset: Linear plot of [DNA]/($\varepsilon_a - \varepsilon_f$) *versus* [DNA] at $\lambda = 278$ nm.

proportion. A closer look at the spectrum (Figure S25) revealed that the formed *cis*-conformer exists as a pair of diastereomers. This is evidenced in the resonances of the two non-equivalent pair of protons of the *p*-cymene, which appear as four signals due to decreased symmetry in the conformer [74]. A plausible mechanism for the substitution reactions in the binuclear complexes is shown in Scheme 3.

3.5. Interactions of chloro complexes Ru7-Ru11 with CT-DNA

3.5.1. UV-vis absorption studies

Spectral changes like those shown in Figure 10 are useful in understanding the nature of the interactions between a metal complex and CT-DNA. This helps in comprehending the molecular mechanism of action of the complexes hence their antitumor activity. In Figure 10, the absorption band between 260 and 400 nm is attributed to charge transfer transitions of type $\pi \rightarrow \pi^*$ or $n \rightarrow \pi^*$, while the bands above 350 nm are assigned to ligand-to-metal charge transfer (LMCT) and MLCT transitions [75]. Thus, the spectral changes due to the MLCT or LMCT band are good indicators of possible

Table 4. The binding constants, quenching constants and number of binding sites for the titration of CT-DNA with Ru(II) complexes.

	UV-Vis titration	Fluorescence quenching titration: CT-DNA/EtBr + Ru(II) complexes				
Complex	K_b (10^5 M^{-1})	K_{sv} (10^3 M^{-1})	k_q (10^{10} M^{-1} s^{-1})	K_{app} (10^5 M^{-1})	K_F (10^3 M^{-1})	n
Ru7	0.83 ± 0.02	0.32 ± 0.01	0.69 ± 0.04	0.99 ± 0.03	0.22 ± 0.01	0.96 ± 0.06
Ru8	8.77 ± 0.10	5.08 ± 0.09	11.04 ± 0.20	5.41 ± 0.12	20.54 ± 0.06	1.26 ± 0.20
Ru9	5.26 ± 0.07	4.44 ± 0.08	9.66 ± 0.10	4.96 ± 0.09	13.74 ± 0.05	1.13 ± 0.10
Ru10	3.99 ± 0.05	4.04 ± 0.05	8.79 ± 0.09	4.55 ± 0.07	7.48 ± 0.05	1.07 ± 0.10
Ru11	1.14 ± 0.02	3.56 ± 0.03	7.74 ± 0.06	4.05 ± 0.05	4.20 ± 0.03	1.01 ± 0.08

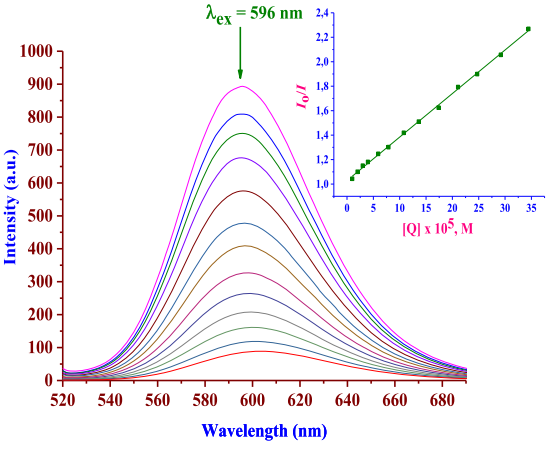

Figure 11. Fluorescence emission spectra of EtBr-CT-DNA bound complex in the presence of increasing concentration of quencher **Ru7**. [EtBr] = 50 μM, [CT-DNA] = 50 μM, [Q] = 0–200 μM. The arrow indicates a decrease in intensity upon increasing [**Ru7**]. Inset: Stern-Volmer linear plot.

(non-covalently or covalently linked) interactions between a complex and the hosting CT-DNA helix.

The interaction of the complexes with CT-DNA was studied by following changes in the absorbance upon incremental addition of CT-DNA to a fixed concentration of each Ru(II) complex. The bands below 350 nm showed a notable hypochromic slight blue-shift of λ_{max} for all complexes as the CT-DNA concentration increased (Figure 10 and S27). This is attributable to an increase in π→π stacking interactions between the aromatic chromophore of the Ru(II) complexes and CT-DNA base pairs as the concentration of the CT-DNA increased. This is consistent with the insertion of the Ru(II) complexes into the base pairs of CT-DNA [76, 77]. The magnitude of the absorption shift depends on the strength of the interactions between them. The intrinsic binding constant (K_b) measures the strength of the interaction of the complexes with the duplex DNA helix and the values obtained are presented in Table 4. The binding constants obtained are large with those of binuclear complexes being higher than that of the mononuclear complex **Ru7**. Thus, the binuclear complexes are more effective in binding to the CT-DNA helix due to favorable electrostatic interactions because of their higher formal charge. This is comparable to what has been reported previously for interactions of CT-DNA with square planar Cu(II) complexes [78]. In addition, the binding constants obtained in this study are comparable to those obtained for other

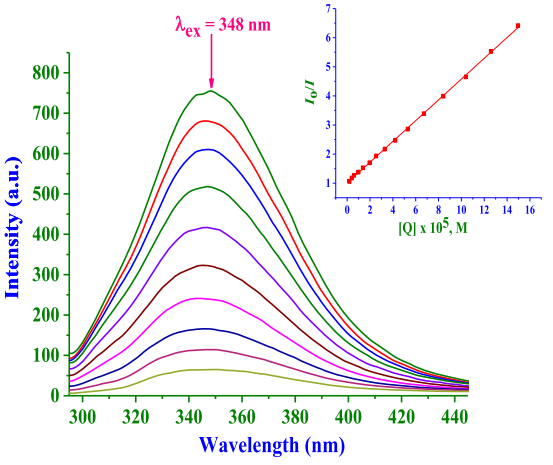

Figure 12. Fluorescence emission spectra of BSA in the presence of increasing concentration of quencher **Ru7**. [BSA] = 0.12 μM, [Q] = 0–130 μM. The arrow indicates a decrease in intensity upon increasing [**Ru7**]. Inset: Stern-Volmer linear plot for the fluorescence titration data.

ruthenium(II) complexes. In these studies, the reported K_b values range between 0.2×10^5 and 5.0×10^6 M^{-1} [79–81].

3.5.2. Fluorescence quenching studies

Since these complexes do not exhibit significant fluorescence at room temperature in the presence of CT-DNA, their binding abilities to CT-DNA could not be determined directly. However, EtBr, a planar cationic dye, fluoresces strongly at $\lambda\sim$ 600 nm in the presence of double-helix CT-DNA where it forms an EtBr-CT-DNA complex. On the contrary, the fluorescence of displaced EtBr (free form) in the non-interfacial volume of Tris buffer is low due to solvent quenching [82, 83]. Thus, when a solution of the EtBr-CT-DNA was titrated with the Ru(II) complexes, the emission intensity around 600 nm was quenched as shown in Figure 11 for the titration of EtBr-CT-DNA solution with **Ru7** (see also Figure S28 for spectral changes for titration of EtBr-CT-DNA solution with **Ru8**–**Ru11**). This was accompanied by a notable red-shift of λ_{max}. The quenching of the fluorescence implies that the Ru(II) complexes are capable of displacing EtBr out of the CT-DNA base pairs through intercalation [84]. The Stern-Volmer plots were linear and the values of K_{sv} are presented in Table 4. The magnitude of quenching constants ($\sim 10^3$ M^{-1}) suggests that all the complexes are strong exchangers of intercalated EtBr from the CT-DNA [85]. Bimolecular quenching rate constants, k_q, were also computed using the same equation and their values are also given in Table 4. Their magnitude (10^{10} $M^{-1}s^{-1}$) is higher than those of known strong bio-polymeric fluorescence quenchers, indicating a dynamic quenching [86, 87]. Thus, the exclusion of EtBr from the CT-DNA base pairs is ultra-fast and possibly irreversible. The fact that the fluorescence of a strong intercalator, EtBr, is quenched by the complexes shows that the interactions are irreversible. It also implies that a significant fraction of its molecules is relegated into the bulk of the solution, where their emission is immediately quenched by solvent molecules. The apparent binding constant (K_{app}), binding constant (K_F) and the number of binding sites (n) values are presented in Table 4

Table 5. Quenching constants (k_{sv}), bimolecular quenching rate constants (k_q), binding constants (K_F) and number of binding sites (n) for the titration of BSA with the Ru(II) complexes **Ru7–Ru11**.

Complex	K_{sv} (10^4 M^{-1})	k_q (10^{10} M^{-1} s^{-1})	K_F (10^5 M^{-1})	n
Ru7	3.57 ± 0.03	1.91 ± 0.02	0.19 ± 0.06	0.93 ± 0.04
Ru8	9.40 ± 0.10	5.03 ± 0.10	6.80 ± 0.30	1.04 ± 0.10
Ru9	9.16 ± 0.09	4.91 ± 0.09	2.85 ± 0.20	1.00 ± 0.10
Ru10	8.97 ± 0.07	4.80 ± 0.05	0.81 ± 0.20	0.97 ± 0.09
Ru11	8.82 ± 0.05	4.73 ± 0.03	0.35 ± 0.10	0.90 ± 0.06

while straight-line plots of $\log(I_o-I)/I$ *versus* [Q] for all the complexes are given in Figure S29. The values of n were found to be ~1 for all the five complexes, indicating that these complexes are bound to CT-DNA in a 1:1 mole ratio.

The magnitude of the binding constants and quenching rate constants decreases according to the ability of the complexes to intercalatively displace EtBr of the base pairs: **Ru8** > **Ru9** > **Ru10** > **Ru11** > **Ru7**. Also, the results are in excellent agreement with data obtained from the UV-vis spectral studies, signifying that the complexes interact non-covalently with CT-DNA in a favorable way.

3.5.3. BSA interactions

The interaction of the chloro complexes (**Ru7**–**Ru11**) with BSA was studied by monitoring the quenching of the emission band of the aromatic amino acid residues (tryptophan, tyrosine, and phenylalanine) of BSA by the complexes. This was done to gain insight into the binding affinities of the complexes to BSA. As shown in Figure 12, a decrease in emission intensity with a prominent blue-shift was noticed at $\lambda = 348$ nm when incremental amounts of quencher (Ru(II) complexes) were added to the BSA solution, indicating that the interactions between BSA and the complexes exist. The observed blue shifts for **Ru7** (3 nm), **Ru8** (5 nm), **Ru9** (3 nm), **Ru10** (7 nm), and **Ru11** (3 nm) are due to increase in hydrophobicity of the microenvironment around the tryptophan in the BSA. This leads to enhanced interactions between the BSA and the complexes [88]. Spectral changes for the other complexes are given in Figure S30. The spectral data was fitted into the Stern-Volmer equation which gave quenching constant, K_{sv}, from the slopes of plots of I_o/I *versus* [Q] (see inset of Figure 12 (for **Ru7**) and Figure S31). The quenching constants (K_{sv}), bimolecular quenching rate constants (k_q), binding constants (K_F) and number of binding sites (n) are presented in Table 5. The magnitude of k_q is found to be in the range of 2–5 × 10^{10} $M^{-1}s^{-1}$, suggesting a dynamic quenching [86]. The n values for all the complexes are ~1, indicating that the complexes are bound to BSA in a 1:1 ratio at each active binding site.

The data in Table 5 show that these complexes bind favorably with the BSA protein in decreasing order: **Ru8** > **Ru9** > **Ru10** > **Ru11** > **Ru7**. The trend is the same to what was observed for their interaction of the complexes with CT-DNA. This suggests the same mode of interactions (*i.e.* docking of the complexes at the appropriate and active receptor pockets on the BSA). From the data presented in Tables 4 and 5, the complexes show good binding affinities for both CT-DNA and BSA. Monometallic complex **Ru7** showed a weak binding compared to binuclear complexes **Ru8**–**Ru11**, probably due to high formal positive charges of the latter as well as synergetic effects at the metal centers due to the bridging ligands. Complex **Ru8** showed the highest binding ability compared to the other binuclear complexes, which is attributable to its

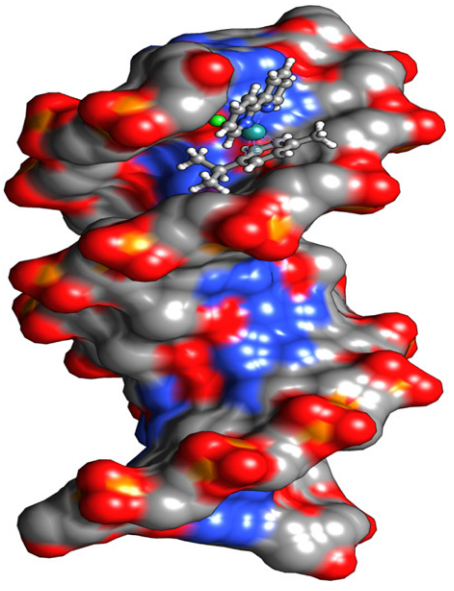

Figure 13. Computational docking model illustrating the interactions of **Ru7** with B-DNA duplex.

planarity and size of the bridge. The bipyrimidine bridging ligand in **Ru8** is planar and the smallest in size, both factors promote it to stack and bind more easily to the CT-DNA or BSA, while the other bridging ligands are not as planar. The data from the binding studies corroborate the observed reactivity trends for the aqua substitution in the aqua complexes using S-donor nucleophiles.

3.5.4. Molecular docking with B-DNA

Complexes **Ru7**–**Ru11** were docked onto DNA to obtain a theoretical insight into their surface molecular interactions, probable binding sites and preferred orientations with DNA duplex. The minimum energy of the docked poses (Figure 13 for **Ru7** and Figure S32 for other complexes) revealed that these complexes fitted into the curved contour of the B-DNA located in the minor groove within the G–C (∼13.4 Å) base sequence. The relative magnitude of the binding energy of the complexes when docked to DNA was found to be −260.84, −285.73, −310.11, −292.48, and −314.84 kJ mol^{-1} for **Ru7**, **Ru8**, **Ru9**, **Ru10**, and **Ru11**, respectively. **Ru7** (a mononuclear complex) has the least relative binding energy compared to the binuclear complexes. **Ru11** showed the highest binding affinity to B-DNA compared to the other binuclear complexes. This can be attributed to the two methyl substituents present in its bridging ligand.

The aromatic heterocyclic rings of the non-leaving ligands of all complexes stabilize the stacking interactions with DNA base pairs, leading to favorably strong van der Waals interactions. The hydrophobic contacts of the ligands of the complexes also interact with the non-polar functional groups within the minor groove of B-DNA to produce stable Ru-DNA non-covalent complexes. Small molecules such as these complexes used in this study preferentially interact with groups in the minor groove according to a perfect fit-cooperative non-repulsive model.

4. Conclusion

The substitution reactivity of the aqua complexes **Ru1**–**Ru6** investigated is strongly dependant on the inherent stereo-electronic properties of the coordinated chelating or bridging ligand. The reactivity of the binuclear complexes is also influenced by the intermetallic distance; as the distance increases the reactivity decreases due to reduced global delocalization of charge with the linking bridge between the metal centers. Two geometric isomeric products are formed in the substitution reactions of the binuclear complexes. The mode of activation for the substitution of the aqua ligands from the complexes is associative. On the other hand, the chloro complexes **Ru7**–**Ru11** showed strong intercalative binding with CT-DNA in which they quenched the florescence emission of the EtBr-CT-DNA complex. The binuclear complexes showed a greater binding affinity for both CT-DNA and BSA due to their higher charge and synergetic effect from the bridging ligand. Owing to its planarity and size, **Ru8** had the highest binding ability for CT-DNA and BSA. The great affinity of the complexes to bind BSA in its hydrophobic regions opens a possibility for target drug delivery by these Fe(III) shuttling protein to tumor (hypoxia) cells, which are in hyper demand of Fe(III), an ion mimic of these complexes.

Acknowledgements

We thank Craig Grimmer and Caryl Janse van Rensburg for characterization of the complexes.

Disclosure statement

No potential conflict of interest was reported by the authors.

Funding

We gratefully acknowledge the financial support accorded to Gershom Mutua by Masinde Muliro University of Science and Technology (Kenya) and University of KwaZulu-Natal (South Africa).

ORCID

Deogratius Jaganyi http://orcid.org/0000-0003-4499-6877

References

[1] W.H. Ang, P.J. Dyson. *Eur. J. Inorg. Chem.*, **2006**, 4003 (2006).
[2] I. Kostova. *Curr. Med. Chem.*, **13**, 1085 (2006).
[3] E.S. Antonarakis, A. Emadi. *Cancer Chemother. Pharmacol.*, **66**, 1 (2010).
[4] C.S. Allardyce, P.J. Dyson. *Plat. Met. Rev.*, **45**, 62 (2001).
[5] Y.K. Yan, M. Melchart, A. Habtemariam, P.J. Sadler. *Chem. Commun.*, 4764 (2005).
[6] J. Furrer, G. Süss-Fink. *Coord. Chem. Rev.*, **309**, 36 (2016).

[7] M.V. Babak, W.H. Ang. In *Metallo-Drugs: Development and Action of Anticancer Agents*, A. Sigel, H. Sigel, E. Freisinger, R. K. O. Sigel (Eds.), pp. 171–198., Berlin, Boston: De Gruyter (2018).
[8] R.E. Morris, R.E. Aird, P. del Socorro Murdoch, H. Chen, J. Cummings, N.D. Hughes, S. Parsons, A. Parkin, G. Boyd, D.I. Jodrell, P.J. Sadler. *J. Med. Chem.*, **44**, 3616 (2001).
[9] M.G. Mendoza-Ferri, C.G. Hartinger, R.E. Eichinger, N. Stolyarova, K. Severin, M.A. Jakupec, A.A. Nazarov, B.K. Keppler. *Organometallics*, **27**, 2405 (2008).
[10] M.G. Mendoza-Ferri, C.G. Hartinger, M.A. Mendoza, M. Groessl, A.E. Egger, R.E. Eichinger, J.B. Mangrum, N.P. Farrell, M. Maruszak, P.J. Bednarski, F. Klein, M.A. Jakupec, A.A. Nazarov, K. Severin, B.K. Keppler. *J. Med. Chem.*, **52**, 916 (2009).
[11] G. Süss-Fink. *Dalton Trans.*, **39**, 1673 (2010).
[12] A.A. Nazarov, J. Risse, W.H. Ang, F. Schmitt, O. Zava, A. Ruggi, M. Groessl, R. Scopelitti, L. Juillerat-Jeanneret, C.G. Hartinger, P.J. Dyson. *Inorg. Chem.*, **51**, 3633 (2012).
[13] K.J. Kilpin, P.J. Dyson. *Chem. Sci.*, **4**, 1410 (2013).
[14] W.H. Ang, A. Casini, G. Sava, P.J. Dyson. *J. Organomet. Chem.*, **696**, 989 (2011).
[15] P. Čanović, A.R. Simović, S. Radisavljević, I. Bratsos, N. Demitri, M. Mitrović, I. Zelen, ŽD. Bugarčić. *J. Biol. Inorg. Chem.*, **22**, 1007 (2017).
[16] O. Nováková, A.A. Nazarov, C.G. Hartinger, B.K. Keppler, V. Brabec. *Biochem. Pharmacol.*, **77**, 364 (2009).
[17] J. Reedijk. *Proc. Natl. Acad. Sci. USA*, **100**, 3611 (2003).
[18] J. Reedijk. *Chem. Rev.*, **99**, 2499 (1999).
[19] F. Wang, H. Chen, J.A. Parkinson, P.D.S. Murdoch, P.J. Sadler. *Inorg. Chem.*, **41**, 4509 (2002).
[20] S. Schäfer, I. Ott, R. Gust, W.S. Sheldrick. *Eur. J. Inorg. Chem.*, **2007**, 3034 (2007).
[21] A.A. Nazarov, S.M. Meier, O. Zava, Y.N. Nosova, E.R. Milaeva, C.G. Hartinger, P.J. Dyson. *Dalton Trans.*, **44**, 3614 (2015).
[22] M. Ganeshpandian, R. Loganathan, E. Suresh, A. Riyasdeen, M.A. Akbarsha, M. Palaniandavar. *Dalton Trans.*, **43**, 1203 (2014).
[23] S. Thota, S. Vallala, R. Yerra, D.A. Rodrigues, N.M. Raghavendra, E.J. Barreiro. *Int. J. Biol. Macromol.*, **82**, 663 (2016).
[24] M. Ganeshpandian, M. Palaniandavar, A. Muruganantham, S.K. Ghosh, A. Riyasdeen, M.A. Akbarsha. *Appl. Organometal. Chem.*, **32**, e4154 (2018).
[25] T. Khamrang, R. Kartikeyan, M. Velusamy, V. Rajendiran, R. Dhivya, B. Perumalsamy, M.A. Akbarsha, M. Palaniandavar. *RSC Adv.*, **6**, 114143 (2016).
[26] A.M. Pizarro, A. Habtemariam, P.J. Sadler. In *Medicinal Organometallic Chemistry. Topics in Organometallic Chemistry*, G. Jaouen, N. Metzler-Nolte (Eds.),Vol. **32**, pp. 21–56., Springer, Berlin (2010).
[27] H.A. Goodwin, F. Lions. *J. Am. Chem. Soc.*, **82**, 5013 (1960).
[28] P. Govindaswamy, J. Canivet, B. Therrien, G. Süss-Fink, P. Štěpnička, J. Ludvík. *J. Organomet. Chem.*, **692**, 3664 (2007).
[29] A. Singh, N. Singh, D.S. Pandey. *J. Organomet. Chem.*, **642**, 48 (2002).
[30] R. Lalrempuia, M.R. Kollipara. *Polyhedron*, **22**, 3155 (2003).
[31] B. Therrien, G. Süss-Fink, P. Govindaswamy, C. Saïd-Mohamed. *Polyhedron*, **26**, 4065 (2007).
[32] L. Colina-Vegas, W. Villarreal, M. Navarro, C.R. de Oliveira, A.E. Graminha, P.I.D.S. Maia, V.M. Deflon, A.G. Ferreira, M.R. Cominetti, A.A. Batista. *J. Inorg. Biochem.*, **153**, 150 (2015).
[33] L. Bíró, A.J. Godó, Z. Bihari, E. Garribba, P. Buglyó. *Eur. J. Inorg. Chem.*, **2013**, 3090 (2013).
[34] OriginPro 9.1. OriginLab Corporation, Northampton, MA.01060, United States, 2014 1800-969-7720. *www.OriginLab.com*.
[35] ŽD. Bugarčić, B.V. Petrović, R. Jelić. *Transit. Met. Chem.*, **26**, 668 (2001).
[36] A. Hofmann, D. Jaganyi, O.Q. Munro, G. Liehr, R. van Eldik. *Inorg. Chem.*, **42**, 1688 (2003).
[37] J. Marmur. *J. Mol. Biol.*, **3**, 208 (1961).
[38] A. Pyle, J. Rehmann, R. Meshoyrer, C. Kumar, N. Turro, J.K. Barton. *J. Am. Chem. Soc.*, **111**, 3051 (1989).

[39] O. Stern, M. Volmer. *Phys. Z.*, **20**, 183 (1919).
[40] D.P. Heller, C.L. Greenstock. *Biophys. Chem.*, **50**, 305 (1994).
[41] M. Lee, A.L. Rhodes, M.D. Wyatt, S. Forrow, J.A. Hartley. *Biochemistry*, **32**, 4237 (1993).
[42] E. Alarcon, A. Aspée, M. Gonzalez-Bejar, A. Edwards, E. Lissi, J. Scaiano. *Photochem. Photobiol. Sci.*, **9**, 861 (2010).
[43] T. Larsson, M. Wedborg, D. Turner. *Anal. Chim. Acta*, **583**, 357 (2007).
[44] K.M. Elkins, M.A. Dickerson, E.M. Traudt. *J. Inorg. Biochem.*, **105**, 1469 (2011).
[45] M. Frisch, G. Trucks, H. Schlegel, G. Scuseria, M. Robb, J. Cheeseman, G. Scalmani, V. Barone, B. Mennucci, G. Petersson. *Gaussian 09, Revision D. 01*, Gaussian, Inc., Wallingford, CT (2009).
[46] J. Li, L.-C. Xu, J.-C. Chen, K.-C. Zheng, L.-N. Ji. *J. Phys. Chem. A*, **110**, 8174 (2006).
[47] R.G. Parr, L.V. Szentpaly, S. Liu. *J. Am. Chem. Soc.*, **121**, 1922 (1999).
[48] G. Macindoe, L. Mavridis, V. Venkatraman, M.-D. Devignes, D.W. Ritchie. *Nucleic Acids Res.*, **38**, W445 (2010).
[49] C.F. Macrae, I.J. Bruno, J.A. Chisholm, P.R. Edgington, P. McCabe, E. Pidcock, L. Rodriguez-Monge, R. Taylor, J.V.D. Streek, P.A. Wood. *J. Appl. Crystallogr.*, **41**, 466 (2008).
[50] H.R. Drew, R.M. Wing, T. Takano, C. Broka, S. Tanaka, K. Itakura, R.E. Dickerson. *Proc. Natl. Acad. Sci. USA*, **78**, 2179 (1981).
[51] E.F. Pettersen, T.D. Goddard, C.C. Huang, G.S. Couch, D.M. Greenblatt, E.C. Meng, T.E. Ferrin. *J. Comput. Chem.*, **25**, 1605 (2004).
[52] D. Jaganyi, A. Hofmann, R. van Eldik. *Angew. Chem. Int. Ed.*, **40**, 1680 (2001).
[53] T. Soldatović, S. Jovanović, ŽD. Bugarčić, R. van Eldik. *Dalton Trans.*, **41**, 876 (2012).
[54] A.F. Peacock, A. Habtemariam, S.A. Moggach, A. Prescimone, S. Parsons, P.J. Sadler. *Inorg. Chem.*, **46**, 4049 (2007).
[55] A. Mambanda, D. Jaganyi. *Dalton Trans.*, **41**, 908 (2012).
[56] A. Hofmann, R. van Eldik. *Dalton Trans.*, 2979 (2003).
[57] L. Bíró, E. Farkas, P. Buglyó. *Dalton Trans.*, **41**, 285 (2012).
[58] K.J. Kilpin, S.M. Cammack, C.M. Clavel, P.J. Dyson. *Dalton Trans.*, **42**, 2008 (2013).
[59] C. Knorrs, H.D. Gafney, A.D. Baker, C. Braunstein, T.C. Strekas. *J. Raman Spectrosc.*, **14**, 32 (1983).
[60] J. Cooper, D. MacQueen, J. Petersen, D.W. Wertz. *Inorg. Chem.*, **29**, 3701 (1990).
[61] S.M. Molnar, K.R. Neville, G.E. Jensen, K.J. Brewer. *Inorg. Chim. Acta*, **206**, 69 (1993).
[62] K.J. Brewer, W.R. Murphy, Jr, J.D. Petersen. *Inorg. Chem.*, **26**, 3376 (1987).
[63] S.C. Rasmussen, M.M. Richter, E. Yi, H. Place, K.J. Brewer. *Inorg. Chem.*, **29**, 3926 (1990).
[64] A.R. Katritzky, C.A. Ramsden, J.A. Joule, V.V. Zhdankin. *Handbook of Heterocyclic Chemistry*, pp. 45–48, Elsevier Ltd., Amsterdam (2010).
[65] M.M. Richter, K.J. Brewer. *Inorg. Chem.*, **32**, 5762 (1993).
[66] L.M. Vogler, C. Franco, S.W. Jones, K.J. Brewer. *Inorg. Chim. Acta*, **221**, 55 (1994).
[67] F. Baumann, A. Stange, W. Kaim. *Inorg. Chem. Commun.*, **1**, 305 (1998).
[68] M. Das, S.E. Livingstone. *Dalton Trans.*, 452 (1975).
[69] T. Bugarcic, A. Habtemariam, R.J. Deeth, F.P. Fabbiani, S. Parsons, P.J. Sadler. *Inorg. Chem.*, **48**, 9444 (2009).
[70] L. Dadci, H. Elias, U. Frey, A. Hoernig, U. Koelle, A.E. Merbach, H. Paulus, J.S. Schneider. *Inorg. Chem.*, **34**, 306 (1995).
[71] G.K. Rauth, D. Das, C. Sinha, K. Bag, A. Mahapatra. *Transit. Met. Chem.*, **27**, 639 (2002).
[72] T. Das, B. Bera, A. Datta, A. Ghosh. *Transit. Met. Chem.*, **34**, 247 (2009).
[73] A.K. Ghosh, A. Mandal, B.K. Bera, S. Mallick, S. Mondal, P. Karmakar. *ICAIJ*, **5**, 176 (2010).
[74] A. Garci, G. Gupta, C. Dalvit, B. Therrien. *Eur. J. Inorg. Chem.*, **2014**, 5651 (2014).
[75] K. Chichak, U. Jacquemard, N.R. Branda. *Eur. J. Inorg. Chem.*, **2002**, 357 (2002).
[76] E.C. Long, J.K. Barton. *Acc. Chem. Res.*, **23**, 271 (1990).
[77] Q.L. Zhang, J.G. Liu, H. Chao, G.Q. Xue, L.N. Ji. *J. Inorg. Biochem.*, **83**, 49 (2001).
[78] R. Castro-Ramírez, N. Ortiz-Pastrana, A.B. Caballero, M.T. Zimmerman, B.S. Stadelman, A.A.E. Gaertner, J.L. Brumaghim, L. Korrodi-Gregório, R. Pérez-Tomás, P. Gamez, N. Barba-Behrens. *Dalton Trans.*, **47**, 7551 (2018).

[79] R.K. Vuradi, K. Dandu, P.K. Yata, M. Vinoda Rani, R.R. Mallepally, N. Chintakuntla, R. Ch, S.S. Thakur, C.M. Rao, S. Satyanarayana. *New J. Chem.*, **42**, 846 (2018).
[80] S. De, S.R. Chaudhuri, A. Panda, G.R. Jadhav, R.S. Kumar, P. Manohar, N. Ramesh, A. Mondal, A. Moorthy, S. Banerjee, P. Paira, S.K.A. Kumar. *New J. Chem.*, **43**, 3291 (2019).
[81] C. Ravi, R.K. Vuradi, S. Avudoddi, P.K. Yata, V.R. Putta, G. Srinivas, R. Merugu, S. Satyanarayana. *Nucleos. Nucleot. Nucl.*, 1 (2019).
[82] M. Howe-Grant, K.C. Wu, W.R. Bauer, S.J. Lippard. *Biochemistry*, **15**, 4339 (1976).
[83] F.J. Meyer-Almes, D. Porschke. *Biochemistry*, **32**, 4246 (1993).
[84] R.F. Pasternack, E.J. Gibbs, J.J. Villafranca. *Biochemistry*, **22**, 2406 (1983).
[85] J.C. Peberdy, J. Malina, S. Khalid, M.J. Hannon, A. Rodger. *J. Inorg. Biochem.*, **101**, 1937 (2007).
[86] X. Zhao, R. Liu, Z. Chi, Y. Teng, P. Qin. *J. Phys. Chem. B*, **114**, 5625 (2010).
[87] I. Mitra, S. Mukherjee, V.P. Reddy B, B. Misini, P. Das, S. Dasgupta, W. Linert, S.C. Moi. *New J. Chem.* , **42**, 2574 (2018).
[88] U. Kragh-Hansen, F. Hellec, B. de Foresta, M. Le Maire, J.V. Møller. *Biophys. J.*, **80**, 2898 (2001).